

We are IntechOpen, the world's leading publisher of Open Access books Built by scientists, for scientists

6,900

Open access books available

186,000

International authors and editors

200M

Downloads

Our authors are among the

154

Countries delivered to

TOP 1%

most cited scientists

12.2%

Contributors from top 500 universities



WEB OF SCIENCE™

Selection of our books indexed in the Book Citation Index
in Web of Science™ Core Collection (BKCI)

Interested in publishing with us?
Contact book.department@intechopen.com

Numbers displayed above are based on latest data collected.
For more information visit www.intechopen.com



AFM Application in III-Nitride Materials and Devices

Z. Chen¹, L.W. Su², J.Y. Shi², X.L. Wang², C.L. Tang² and P. Gao²

¹Golden Sand River California Corporation, Palo Alto, California

²Lattice Power Corporation, Jiangxi

¹USA

²China

1. Introduction

The nitride family is an exciting material system for optoelectronics industry. Indium nitride (InN), gallium nitride (GaN) and aluminium nitride are all direct bandgap materials, and their energy gaps cover a spectral range from infrared (IR) to deep ultraviolet (UV). This means that by using binary and ternary alloys of these compounds, emission at any visible wavelength should be achievable.

Atomic force microscopy (AFM) is a powerful tool to study the III-nitride surface morphology, crystal growth evolution and devices characteristics. In this chapter, we provide an overview of AFM application in AlInGaN based materials and devices.

Typical surface morphologies of GaN materials characterized by AFM are presented in §1. In additional, three types of threading dislocations, including edge, screw and mixed threading dislocation, are studied by AFM in this section. In §2, V-shape defects and other features in InN, InGaN film and InGaN/GaN multiple quantum wells are summarized. It is not easy to grow high quality AlN and AlGaN films, materials for UV light emitting diode and high electron mobility transistor, which usually have high dislocation density and three dimensional growth mode. Growth condition optimization of high quality, crack-free and smooth Al(Ga)N, with the assistance of AFM, is reviewed in §3. Applications of AFM in GaN based devices are discussed in §4, including the patterned sapphire substrates, as-grown LED surface, backside polished surface, ITO surface investigation.

2. AFM study of GaN

In recent years, the III-nitride-based alloy system has attracted special attention since high-brightness blue, green and white light-emitting diodes (LEDs), and blue laser diodes (LDs) became commercially available.

Good topography and crystal quality of GaN films are some of the key factors to improve devices performance. AFM helps researchers to observe the surface morphology of GaN, to study dislocations in GaN film, and to further understand and optimize the growth condition of the GaN.

2.1 AFM study of GaN surface morphology

Fig. 1(a) is a $10 \times 10 \mu\text{m}^2$ AFM image of typical high-quality, fully coalesced GaN film on sapphire grown by metal organic chemical vapor deposition (MOCVD). Well-defined, uniform and long crystallographic steps could be observed on the surface. The sample topography exhibited atomic terraces with a measured height of 0.3 nm, in close agreement with the 0.26 nm bi-layer spacing of GaN. Fig. 1(b) is $20 \times 20 \mu\text{m}^2$ AFM image of poor-quality, uncoalesced GaN film for comparison. The biggest void (hole) was formed at the coalescence boundaries of the nanoisland growth fronts. The width of the observed hole is up to $2.5 \mu\text{m}$ and the depth could be several microns because the holes result from the poor coalescent at the beginning of the growth.

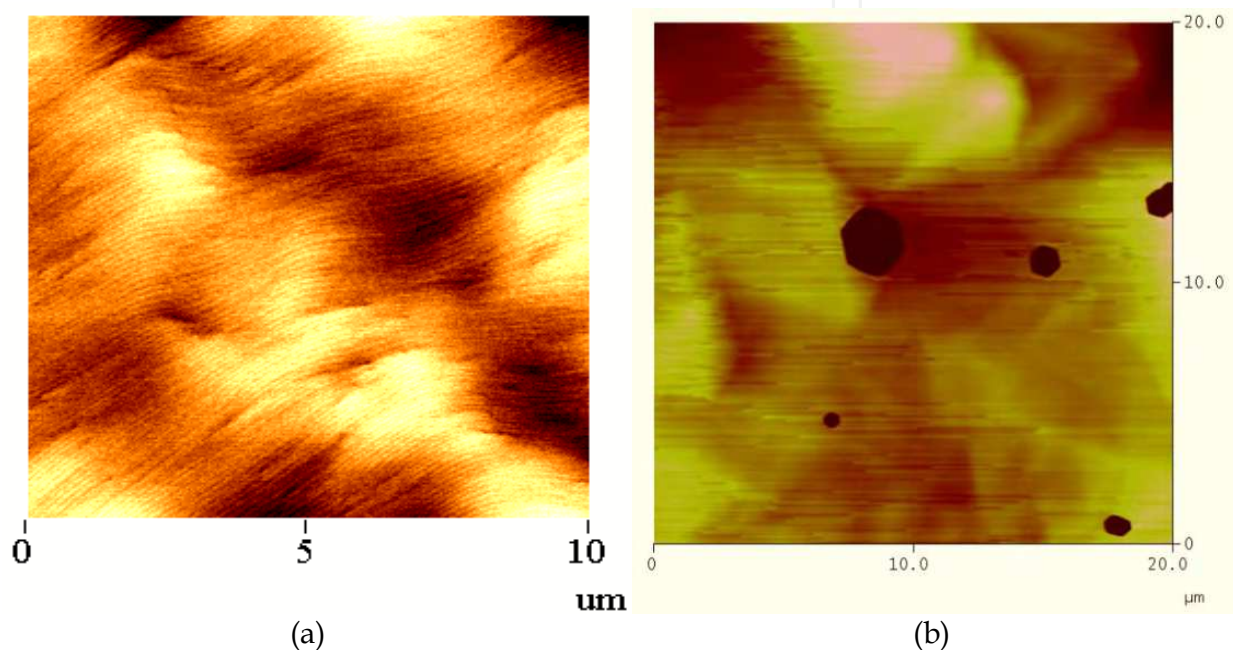


Fig. 1. (a) $10 \times 10 \mu\text{m}^2$ AFM scan of high quality, fully coalesced GaN film; (b) $20 \times 20 \mu\text{m}^2$ AFM scan of un-coalesced GaN film.

The intersection of a screw-component dislocation with the film surface creates an atomic step termination that may lead to spiral step procession and hillock formation (Burton et al 1951). At the top of these hillocks AFM reveals the presence of either single screw or clustered screw and mixed-type dislocations, as shown in Fig. 2(a). The presence of clustered defects with the screw component of the Burgers vector is a reason of formation of the growth hillocks.

Spiral growth hillocks, with pits located at the top and some pits located away from the hillock peaks, are shown in Fig. 2(b). Pits at the center of a spiral growth hillock are expected to have a screw component, while dislocation pits away from hillock peaks without terminated steps are of pure edge character.

2.2 Study of dislocation in GaN by AFM

Fig. 3 is a $2 \times 2 \mu\text{m}^2$ AFM image of a GaN film, in which three kinds of pits of different sizes correspond to three different dislocations were observed. Three types of threading

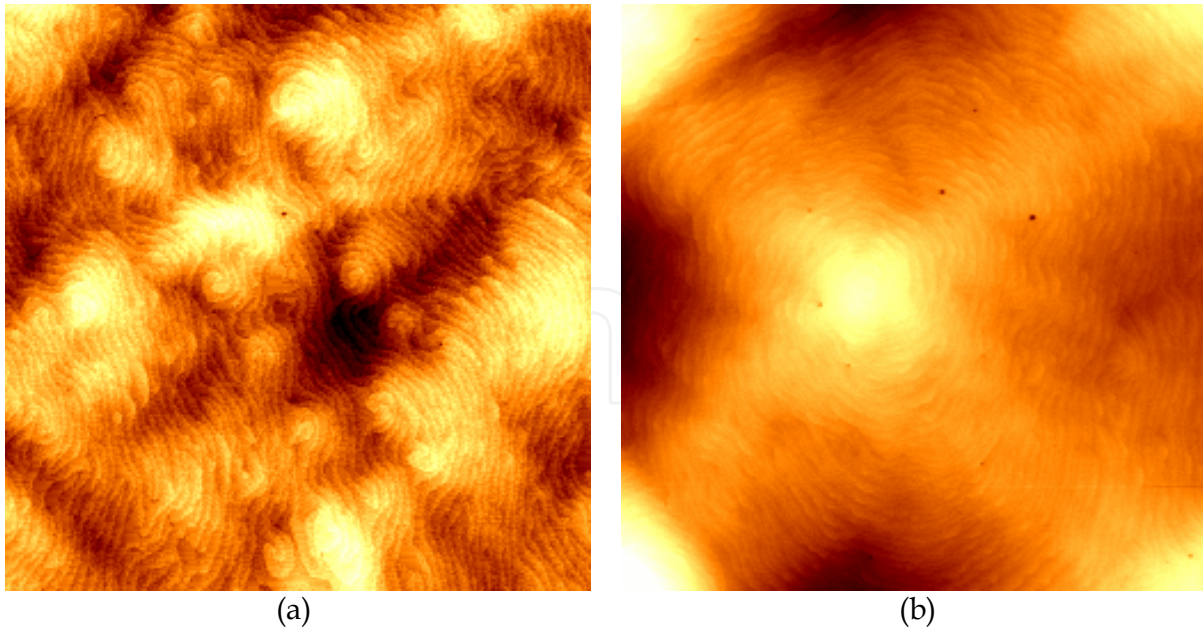


Fig. 2. $5 \times 5 \mu\text{m}^2$ AFM scans of the (a) GaN sample with lot of hillocks; (b) GaN sample with single hillock and several pits.

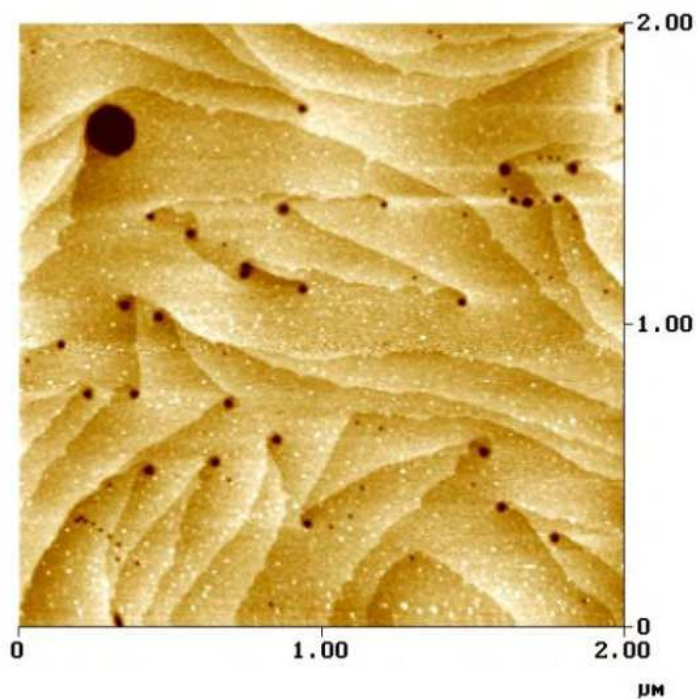


Fig. 3. AFM image of one GaN film showing three types of pits, corresponding to three kinds of dislocations in GaN.

dislocations, edge, screw and mixed types are usually observed in wurtzite GaN epitaxial layers, with the corresponding Burgers vectors, confirmed by TEM (Follstaedt et al. 2003 ; Datta et al. 2004).

$$b_{\text{edge}} = 1/3 [11\bar{2}0]$$

$$b_{\text{mixed}} = 1/3 [11\bar{2}3]$$

$$b_{\text{screw}} = [0001]$$

According to the thermodynamics of pit formation (Sangwal, 1987), it follows that the potential difference ($\Delta\mu$ of a stable nucleus of a pit depends inversely on the elastic energy (E_{el}) of the dislocation: $\Delta\mu = 2\pi^2\Omega\gamma^2 / E_{\text{el}}$ where: E_{el} is elastic energy of dislocation, γ is edge free energy, Ω is molecular volume. The elastic energy value for screw, edge and mixed type of dislocations are:

$$E_{\text{screw}} = Gb^2\alpha$$

$$E_{\text{edge}} = Gb^2\alpha\left(\frac{1}{1-\nu}\right)$$

$$E_{\text{mixed}} = Gb^2\alpha(1 - \nu \cos\theta / (1 - \nu))$$

(where: G is shear modulus, b is Burgers vector, α is geometrical factor, ν is Poisson's constant and θ is the angle between screw and edge components of the Burgers vector of mixed dislocations) (Hull et al., 1984).

Large differences in the magnitude of Burgers vectors, especially between edge type and screw/mixed type dislocations, imply that the size of pits should be different depending on the type of dislocation, i.e. the largest pits are formed on screw-, intermediate size pits on mixed- and the smallest ones on edge-type dislocations (Weyher et al., 2004). The densities of the pits in the sample shown in Fig. 3 with median and larger sizes are $7.5 \times 10^8/\text{cm}^2$, in agreement with the expected density of screw component dislocations. The majority of dislocations are of pure edge character, related to the smallest pits, with a density of $1 \times 10^9/\text{cm}^2$, in agreement with the expected pure edge dislocation density determined by TEM examination.

3. AFM study for In(Ga)N

3.1 V-shape defect in InGaN

Bulk InGaN or InGaN/GaN multiple quantum wells (MQWs) have been used as active layers for near UV, blue, green and white LEDs, laser diodes and solar cells due to the tunable band-gap energy of InGaN, from 0.7 to 3.4 eV through indium composition variation. Therefore it is important to understand the role of microstructural and compositional inhomogeneities in the InGaN layers on the optical emission.

InGaN MQWs structures often have a so-called V-shape defect (Wu et al., 1998; Kim et al., 1998; Northrup et al. 1999; Duxbury et al., 2000; Scholz et al., 2000; Kobayashi et al., 1998) that consists of a threading dislocation terminated by a pit in the shape of an inverted hexagonal pyramid with $[10\bar{1}1]$ sidewalls, as shown in Fig. 4. Pit formation creates 6 equivalent $[10\bar{1}1]$ facets. The depth of the pit is $h=1.63a$. The angle of the hexagonal inverted pyramid defects is 61° , which could be measured accurately by AFM shown in Fig. 4.

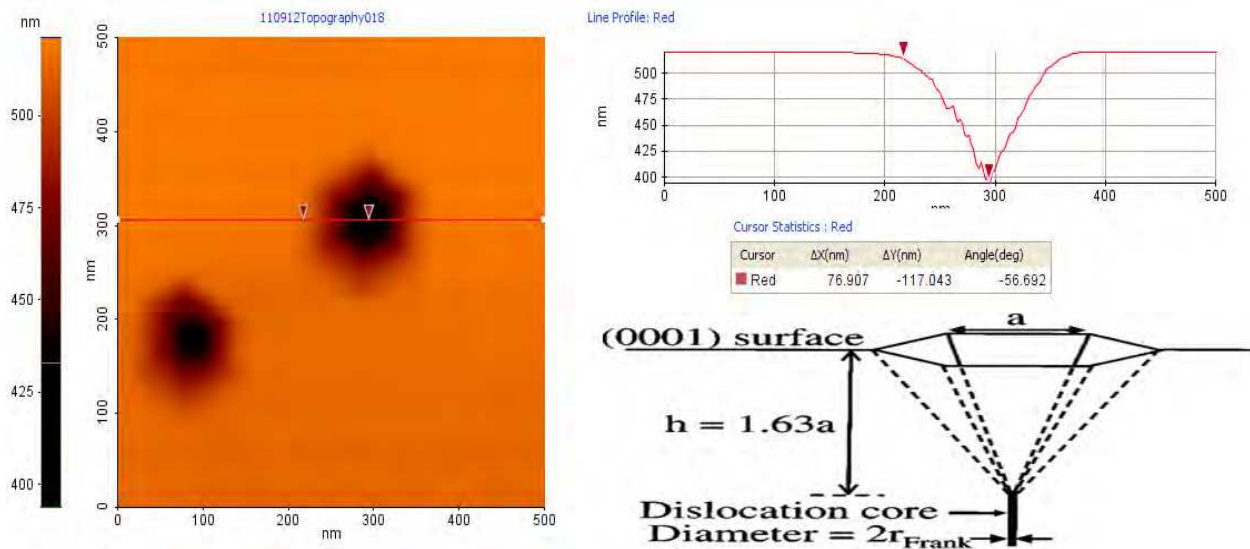


Fig. 4. AFM topography of V-shape defect in InGaN film. A representation of a dislocation terminating in a pit at the (0001) surface is shown.

It is usually accepted that the high defect density in GaN leads to poor optical property and also affects the structural and optical quality of the active layer composed of the InGaN/GaN MQWs. It has been reported that threading dislocations disrupt the InGaN/GaN MQW and initiate the V defect using transmission electron microscopy (TEM) and atomic force microscopy (AFM) (Sharma et al., 2000 ; Lin et al., 2000). Several research groups have reported that there is always a threading dislocation (TD) connected with the bottom of V defect and the cause of V-defect formation is the increased strain energy and the reduced Ga incorporation on the $[10\bar{1}1]$ pyramid planes compared with the $[0001]$ plane (Sun et al., 1997). Cho et al. investigate the V defects in InGaN/GaN MQWs by TEM (Fig. 5) and found that the origin of V defects are not only connected to TD, but also generated from the stacking mismatch boundaries (SMBs) induced by stacking faults (SFs) shown in Fig. 6(a) and 6(b) (Cho et al., 2001).

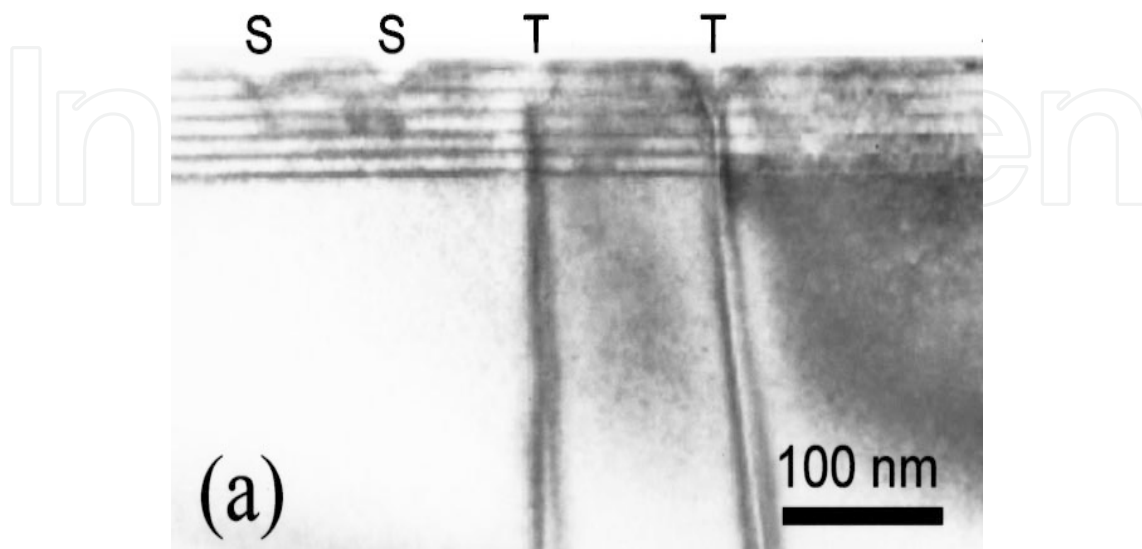


Fig. 5. Cross-sectional bright-field TEM images of the In_{0.3}Ga_{0.7}N/GaN MQWs.

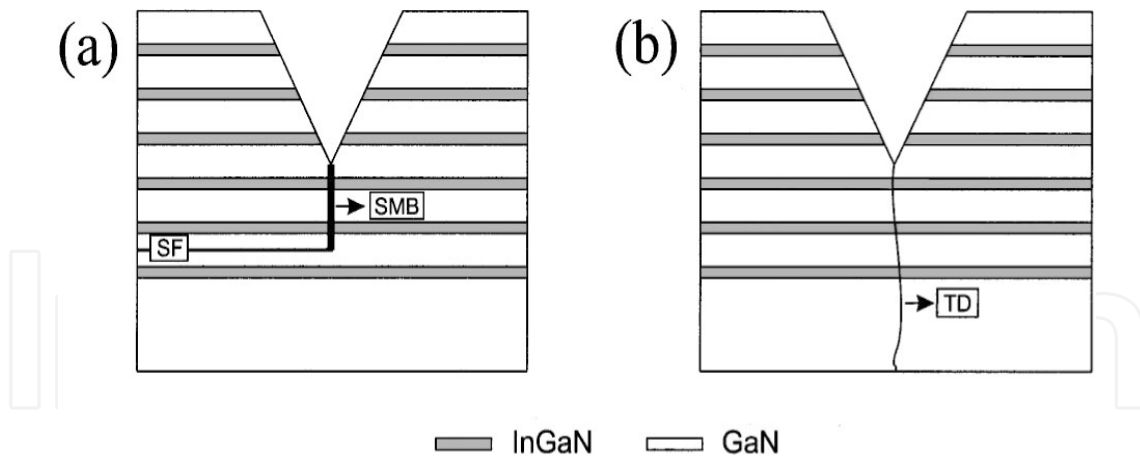


Fig. 6. Schematic models for V-defect formation connected with (a) a threading dislocation and (b) a SMB induced by stacking faults.

The AFM images in Fig. 7 shows the $5 \times 5 \mu\text{m}^2$ scans of the InGaN/GaN superlattice (SL) structure, which is used as the strain release layer in LEDs and LDs. Sample A, with In% composition of 8% is pictured in Fig. 7(a) and sample B, with In% composition of 2% is shown in Fig. 7(b). Remarkable morphological differences are noticeable. A slightly lower density of pits with a wider range of pit diameters is noted for sample A (Fig. 7(a)) when compared to sample B (Fig. 7(b)). In addition, the typical inclusions are shown for sample A as bright, irregular white features. The V-pits density in Fig. 7(a) is around $3 \times 10^8/\text{cm}^2$, with the average diameter of around 120 nm, and inclusion heights up to 120 Å. The defect density in sample B (less Indium) is around $4 \times 10^8/\text{cm}^2$ with diameters in the 50 nm range.

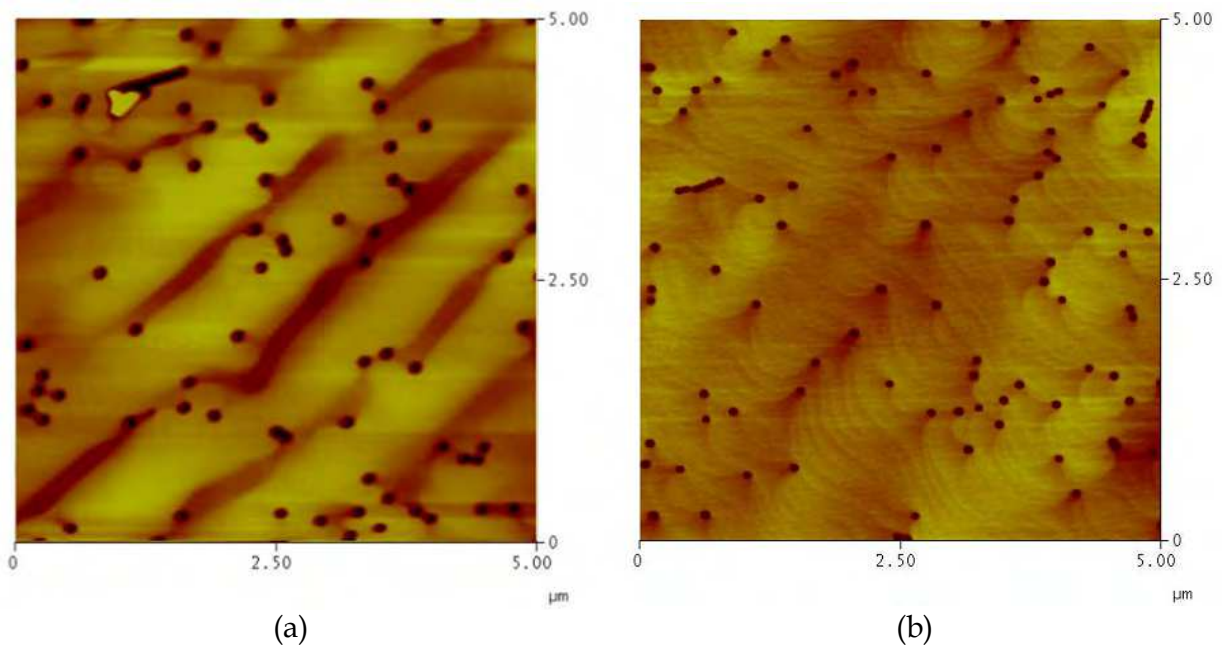


Fig. 7. $5 \times 5 \mu\text{m}^2$ AFM scans of the InGaN/GaN superlattice (SL) structure with (a) indium composition of 7% (b) indium composition of 2%.

The AFM images in Fig. 8 show the $5 \times 5 \mu\text{m}^2$ scans of a InGaN/GaN MQW structure. As previously described in Fig. 4, a V-pit usually connected to a TD and the diameter of the TD

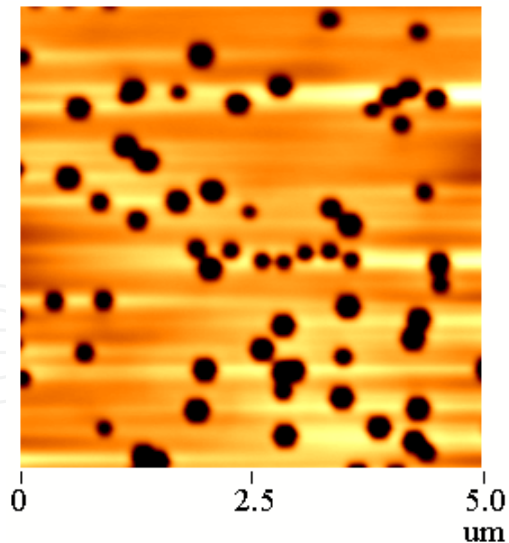


Fig. 8. $5 \times 5 \mu\text{m}^2$ AFM scans of a InGaN/GaN MQW structure. Two kinds of V-defects with different sizes were observed.

should depend on the magnitude of the Burgers vector of dislocations. The bigger TD diameter results in a bigger pit, thus, the bigger V-pits on the InGaN/GaN MQWs are rooted to screw or mixed TD, while the smaller V-pits connected to edge TDs. The diameter of the bigger V-pits in Fig. 8 is about 300 nm, with the density around $1.2 \times 10^8/\text{cm}^2$, corresponding to the density of the screw TD, while diameter and density of the smaller V-pits in Fig. 8 is about 180 nm and $1.0 \times 10^8/\text{cm}^2$, corresponding to the density of the edge TD. The size of the V-pits is bigger than InGaN/GaN SL structure shown in the previous Fig. 7(a) because V-defects grow bigger and bigger with a thicker InGaN layer and a higher Indium composition. The density of the V-pits usually is lower than the TD density in GaN underlayer because not every TD develops to a V-pit. In additional, only one kind of V-pit with the same size was observed for some InGaN/GaN sample, because the V-pits connected to screw TDs is easier to be opened.

3.2 InN growth condition optimization

InN has a band gap value of 0.67–0.8 eV, which potentially extends the spectral range covered by group-III nitrides to the near-infrared. In addition, InN has a very small electron effective mass and a high electron drift velocity (O'Leary et al., 1998). Recent theoretical calculations predict an ultimate room temperature electron mobility for InN to reach 14,000 cm^2/Vs . (Polyakov et al., 2006). However, it is very difficult to grow InN materials due to the thermal instability of InN and the large lattice mismatches between InN and substrates. A high V/III flux ratio and a low growth temperature are usually required to suppress InN decomposition, which often results in unsatisfactory crystal quality and undesired three-dimensional (3D) surfaces roughness. Several technologies have been applied to improve InN film quality and surface morphology. However, AFM has been the most common tools for surface morphology evaluation and improvement.

Fig. 9 is an AFM scan showing the surface morphology of a typical InN film grown by MOCVD on GaN. A low density of large islands with widths up to about 1 μm and heights of 300–400 nm can be observed, which might be indium droplets (Norenberg et al., 2002).

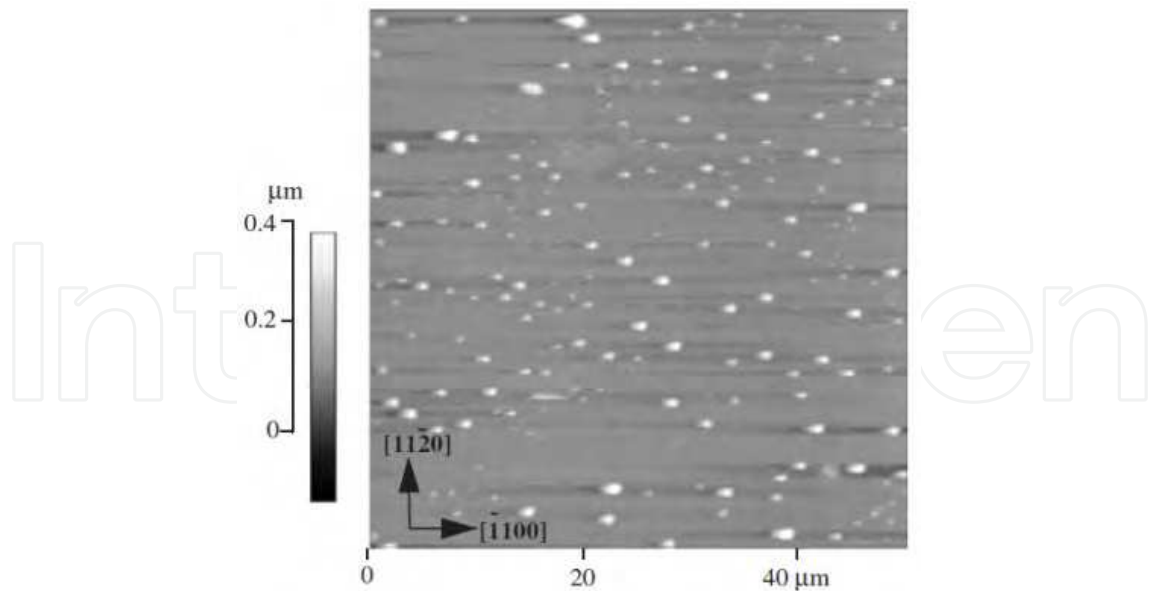


Fig. 9. AFM micrographs of typical InN layer.

InN is usually grown by MBE due to its low growth temperature. Chad et al. grew InN films in two different growth regimes and characterized the surface morphology by AFM, as shown in Fig. 10(a) (the N-rich regime) and Fig. 10(b) (the In-droplet regime). Clear growth steps were observed for InN grown in N-rich regime and Indium droplets were observed when it was grown in the In-droplet regime (Gallinat et al., 2006).

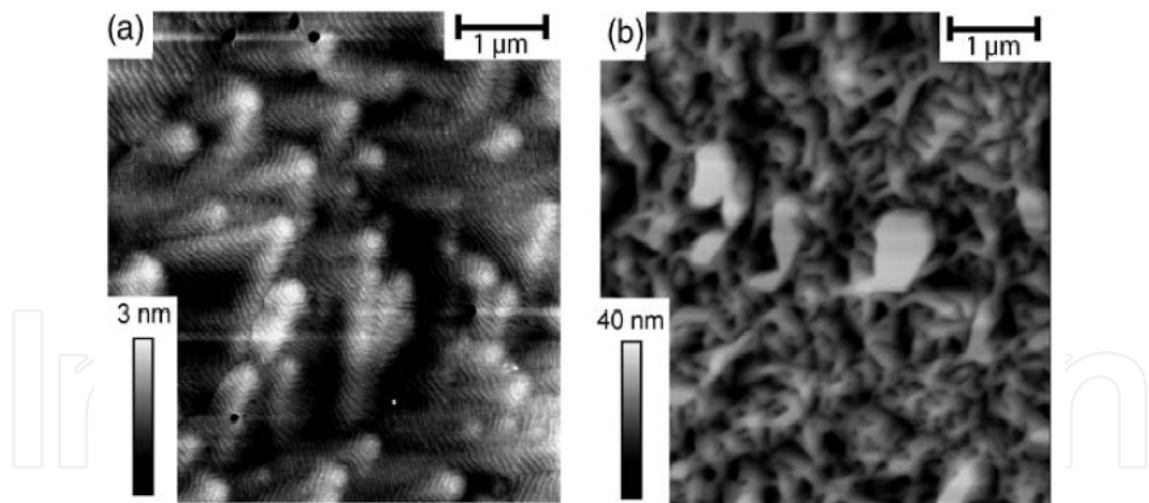


Fig. 10. AFM micrographs of (a) a 1.5- μm -thick InN layer grown in the In-droplet regime and (b) a 1- μm -thick InN layer grown in the N-rich regime.

4. AFM study of Al(Ga)N

4.1 AlN growth condition optimization

Due to its potential for many applications, the growth and characterization of AlN has been a subject of much interest. Great progresses on AlN material growth and device fabrication have been attained. The first electroluminescent emission at wavelength of 200 nm from a p-i-n AlN

homojunction LED operating at 210 nm was realized (Taniyasu et al., 2006). The first AlN metal-semiconductor-metal photodetector with a peak responsivity at 200 nm was obtained (Li et al., 2003). Significant improvement of the AlN crystal quality using Lateral Epitaxial Overgrowth (LEO) of AlN on sapphire substrates was also demonstrated (Chen et al., 2006). This resulted in 214 nm stimulated emission, the shortest wavelength stimulated emission reported in semiconductor materials (Shatalov et al., 2006).

AlN is widely used as the buffer layer for Ultraviolet (UV) Light Emitting Diodes (LED) and High Electron Mobility Transistors (HEMT) grown on SiC substrates currently due to its small lattice constant, wide bandgap and high thermal conductivity (Chen et al. 2009a; Chen et al. 2009b). It is therefore necessary to develop an uncomplicated method for growing high quality, thick and crack-free AlN on SiC substrates. AFM images of the AlN grown in 3D and 2D modes are shown in Figs. 11(a) and 11(b), respectively. Islands are present in Fig. 11(a), showing that this material has a 3D growth mode. Steps with a height difference of one (0001) AlN monolayer can be seen in Fig. 11(b), showing that the growth mode of this material is 2D. The RMS surface roughness of the 3D AlN over $5 \times 5 \mu\text{m}^2$ area is 0.517 nm, while that of the 2D AlN is 0.151 nm.

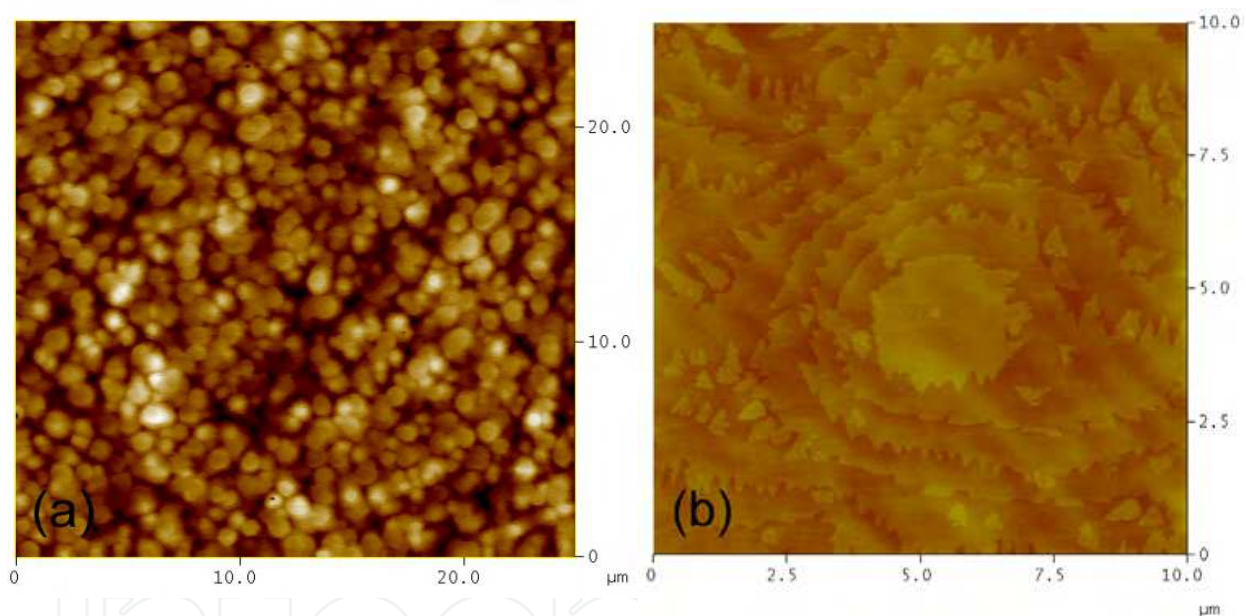


Fig. 11. AFM images of AlN grown at different growth modes: a) three-dimensional, b) two-dimensional.

High quality AlN films were grown by switching between the established 2D and 3D AlN growth modes, a method we call modulation growth (MG) (Chen et al. 2008;). The structure of a MG AlN sample is shown in Fig.12. First, a 300 nm 3D AlN layer was grown on the SiC substrate. Then a 2D 200 nm AlN layer was grown. Subsequently, this 3D-2D period was repeated twice. The total thickness of the resulting film is 1.5 μm . The surface of the AlN grown by 3D-2D modulation growth is very smooth. Fig. 13 shows a $5 \times 5 \mu\text{m}^2$ AFM scan of the surface with an RMS surface roughness of 0.132 nm. Well defined steps and terraces indicate a step-flow growth mode, and can be observed in all parts of the wafer. The height difference between terraces corresponds to one monolayer of (0001) AlN. No step terminations were observed over the scanned area indicating a low density of Threading

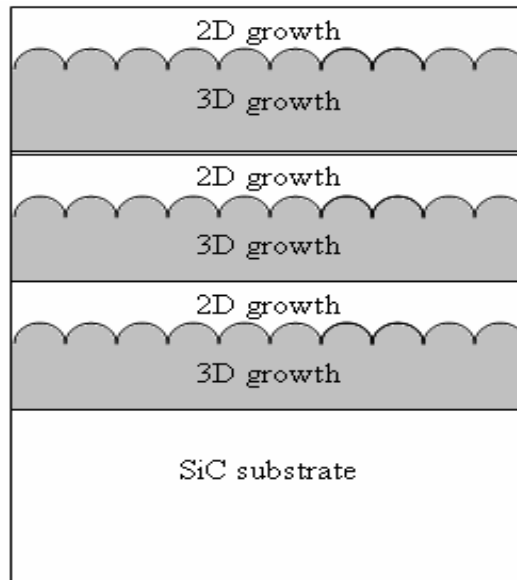


Fig. 12. Schematic of AlN grown with 3D-2D modulation growth method.

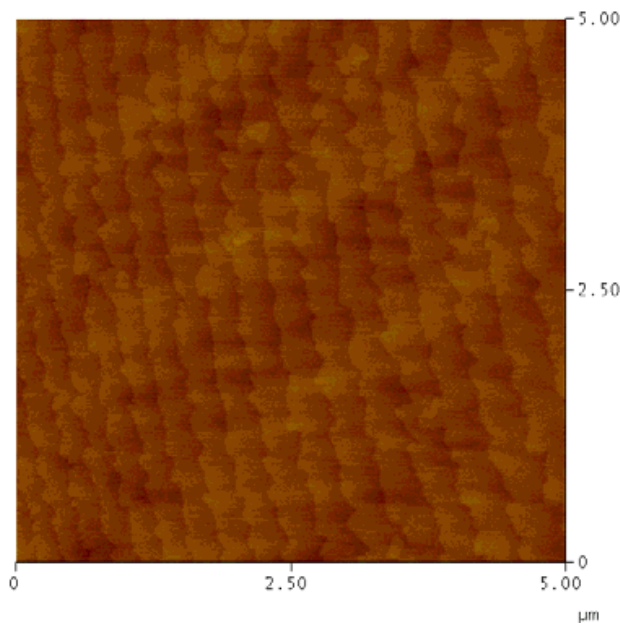


Fig. 13. AFM image of AlN grown with the 3D-2D modulation method.

Dislocation (TD) with screw character, which was confirmed by on-axis and off-axis X-ray rocking curves. The Full Widths at Half Maximum (FWHM) of the (002) and (102) peaks were 86 and 363 arc sec, respectively. The off-axis (105) and (201) peaks were also measured and have FWHM of 225 and 406 arc sec, respectively. The narrow symmetric and asymmetric FWHM of the X-ray data for AlN suggest a low threading dislocation (TD) density, with a small proportion of TDs with screw components.

An atomically flat surface can be obtained when AlN growth is performed at temperatures higher than 1300 °C (Imura et al., 2007). However, the dislocation density is still as high as 1×10^{-10} . Therefore, the crystalline quality of AlN requires further improvement, particularly when it is grown on sapphire substrates.

Epitaxial lateral overgrowth (ELOG) and similar techniques have proved to be an effective method to reduce the TD in GaN (Detchprohm et al., 2001; Weimann et al., 1998) and improve the devices performance. However, ELOG is difficult to undertake with AlN, and even with AlGaN, due to the high sticking coefficient of Al adatom, thus causing a low lateral growth. For the first time, Chen et al. reported the pulsed lateral epitaxial overgrowth (PLOG) of AlN films over shallow grooved sapphire substrates (Chen et al., 2006). The PLOG approach at temperatures around 1150 °C enhances the adatom migration thereby significantly increasing the lateral growth rates. This enables a full coalescence in wing regions as wide as 4 to 10 μm .

In the ELOG process for AlN, first a 0.3- μm -thick AlN layer was grown on the sapphire substrates using a migration-enhanced low pressure MOCVD process. Standard photolithography was then used to form 2 μm wide-masked stripes, with 4-10 μm wide openings oriented along the AlN $\langle 1\bar{1}00 \rangle$ directions. Reactive ion etching was used to remove the AlN and sapphire in the openings area to form 4-10 μm -wide and 0.7- μm -deep trenches. This grooved sapphire/AlN sample served as the template for the subsequent pulsed lateral epitaxial overgrowth. TMA and NH_3 were used as the precursors, and growth was carried out at 1150 °C. For the PLOG process, the NH_3 supplied to the reactor was pulsed (pulse durations 6 to 12 seconds) while the TMA flow was kept constant during the growth.

Fig. 14 shows a cross-sectional SEM image of a fully coalesced PLOG-AlN film with a 4- μm -wide trench (4- μm -wide support mesa). The SEM image clearly shows lateral growth in the $\langle 11\bar{2}0 \rangle$ direction. The sidewall and the top surface are very smooth. A complete triangular void forms upon the trench after the coalescence of the stripes when thickness of the film reaches 6 μm . This indicates the lateral to vertical growth rate ratio is 1:3.

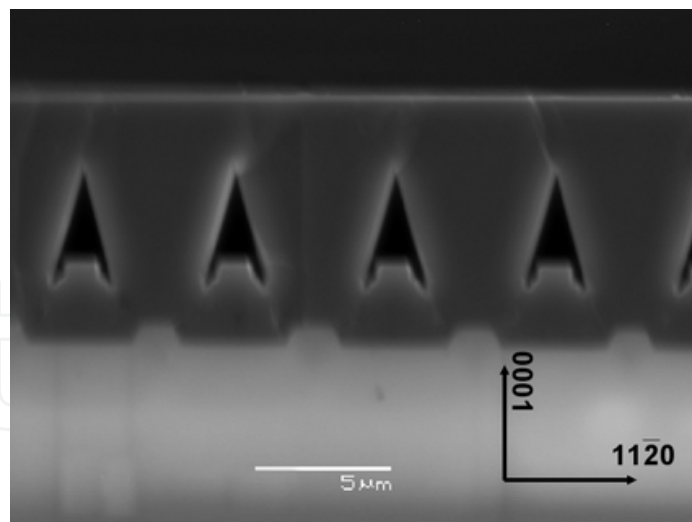


Fig. 14. Cross sectional SEM image of AlN film grown on grooved template by PLOG.

After coalescence, the AlN surface became flat over the whole wafer. A $10 \times 10 \mu\text{m}^2$ atomic force microscopy (AFM) scan shows an RMS surface roughness of 0.5 nm. Fig. 15 shows a $6 \times 6 \mu\text{m}^2$ AFM scan image covering one mask period of the PLOG-AlN surface including both the region directly grown on top of the support mesa and the region laterally grown over the trench. As seen from the well-defined steps and terraces, a two dimensional step-flow growth is dominant over the entire wafer under these PLOG growth conditions.

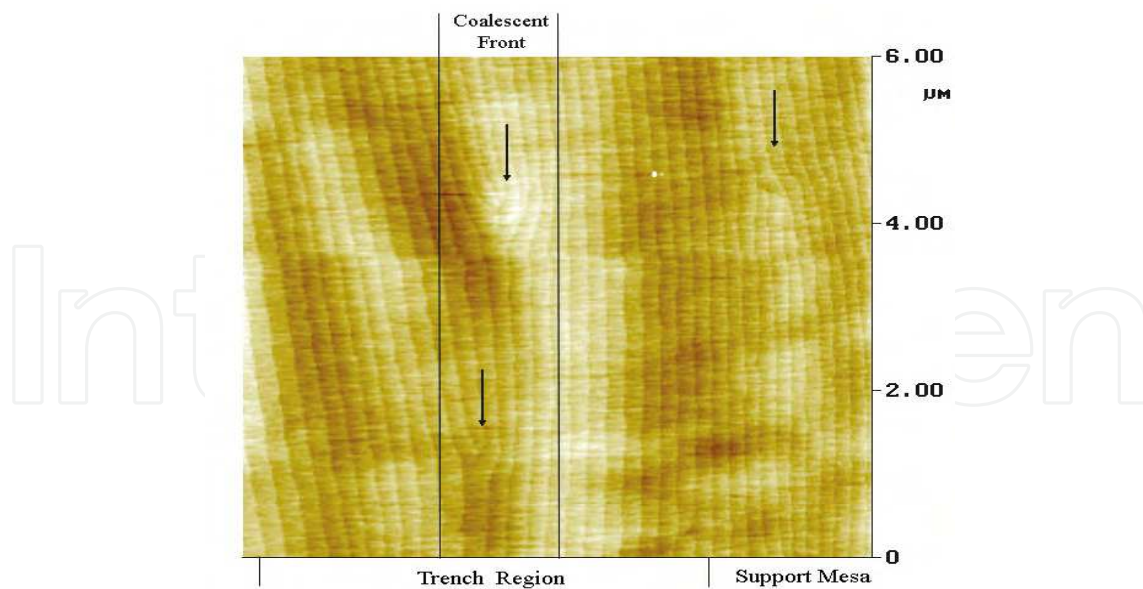


Fig. 15. AFM image acquired from the PLOG-AlN trench and support mesa regions. Arrows point to intersections of dislocations at the surface.

Height differences of 0.27 nm between terraces correspond to one monolayer of (0001) AlN ($c/2=0.25\text{nm}$). The overgrown region has long parallel atomic steps without step terminations, indicating a reduced TD density. At the coalescence point, two threading dislocations marked by arrows are seen in Fig. 15 as step terminations in the AFM image. Another TD is observed in the support area in the same image, implying higher TD density in the support mesa region than that of the trench region. The step termination density, corresponding with either pure screw or mixed screw-edge character, measured by AFM, is $8.3 \times 10^6 \text{cm}^{-2}$ for the scan area shown in Fig. 15.

4.2 AlGa_xN material growth

The growth of Al_xGa_{1-x}N can be carried out on sapphire substrates with a thin low temperature (LT) AlN nucleation layer (Wickenden et al., 1998; Wang et al., 2007; Koide et al., 1988) or thick high temperature (HT) AlN template (Sun et al., 2004; Mayes et al., 2004; Fischer et al., 2004). Grandusky et al. studied the effect of LT-AlN nucleation layer growth conditions for the growth of high quality Al_xGa_{1-x}N layers on sapphire (Grandusky et al., 2007). The conditions of the LT AlN had a dramatic effect on the morphology and crystalline quality of the overgrown Al_xGa_{1-x}N layers. The effect of growth temperature and thickness of the LT AlN nucleation layers on the overgrown Al_{0.5}Ga_{0.5}N is shown in Fig. 16. Fig. 16(a) shows a smooth surface with a RMS roughness of 1 nm over $10 \times 10 \mu\text{m}$, whereas Figs. 16(b) and (c) show rough surfaces with 3D crystallites clearly evident. As demonstrated in Fig. 16, extreme changes in the surface morphology are seen with further increase in temperature of the nucleation layer (NL). For a lower growth temperature of 525 °C for the AlN NL, little change was seen in the surface morphology. The best surface morphology was the sample with a thickness of 15 nm as can be seen from Figs. 16(d)–(f). Large AlGa_xN surface crystallites were observed when the nucleation layer was too thin, as shown in Fig. 16(d). When the layer was thicker than 15 nm, slight roughening of the surface could be seen in Fig. 16(f), as well as a broadening of the (0002) rocking curve.

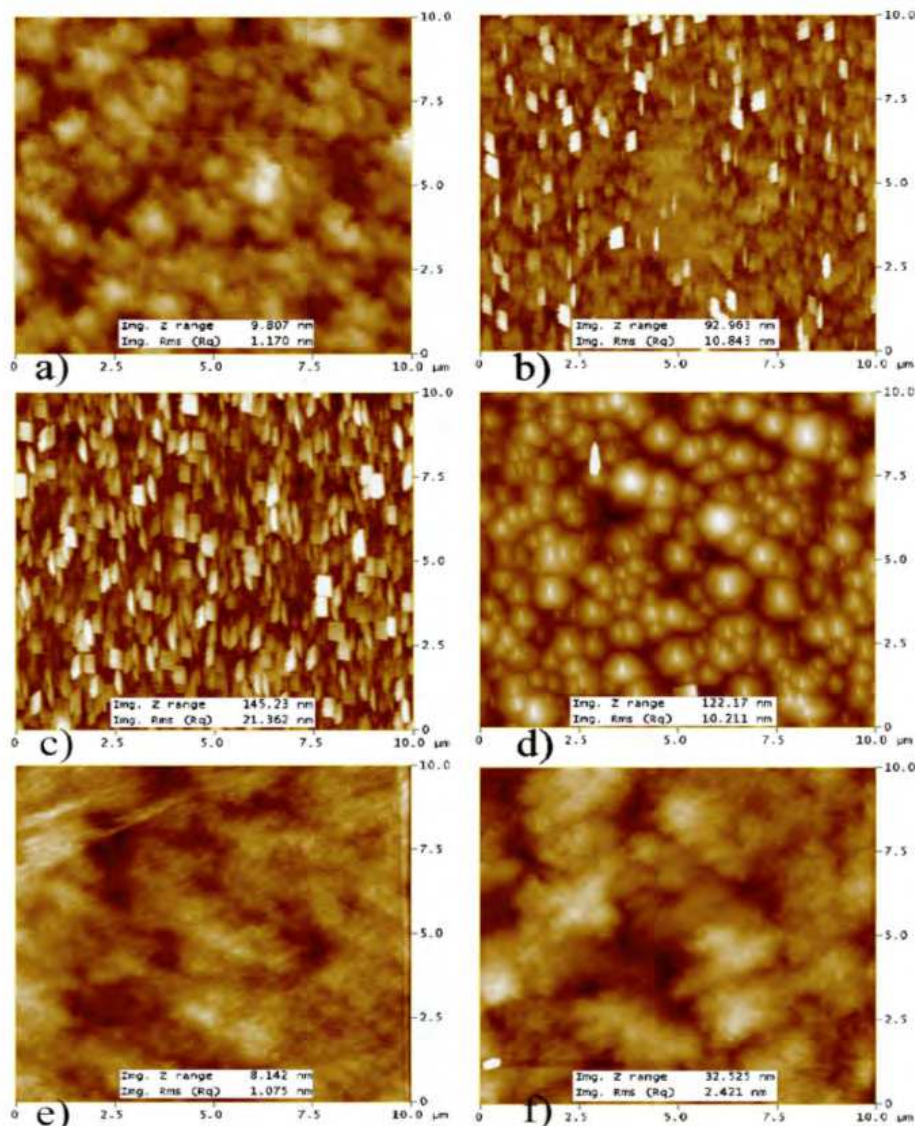


Fig. 16. AFM scans of 500 nm thick $\text{Al}_{0.5}\text{Ga}_{0.5}\text{N}$ grown on a 15 nm AlN nucleation layer grown at (a) 625 °C, (b) 650 °C, and (c) 675 °C and on a low temperature 525 °C AlN NL with thicknesses of (d) 10 nm, (e) 15 nm, and (f) 30 nm.

Subsequently, it was observed by AFM that the direct growth of a 1 μm layer of AlGaN on AlN homoepitaxial layers always results in a roughened morphology. To facilitate heteroepitaxial strain relaxation while preserving structural quality, Z. Ren et al. adopted a design of step-graded layers consisting of three superlattices (SLs 1, 2, and 3) with average Al compositions of 0.90, 0.73, and 0.57. Each SL was composed of ten periods of $\text{Al}_x\text{Ga}_{1-x}\text{N}$ (150 Å)/ $\text{Al}_y\text{Ga}_{1-y}\text{N}$ (150 Å) ($x/y=1.0/0.8, 0.8/0.65, \text{ and } 0.65/0.50$) (Ren et al., 2007). Surface morphology after the growth of SL 1 (Figs. 17(a) and (d)) and SL 2 (Figs. 17(b) and (e)) indicates that pseudomorphic growth persists with an atomically smooth surface under a step-flow growth mode. During the growth of SL 3, surface morphology underwent a fundamental change with the appearance of large 1–2 μm plateaus or platelets separated by deep trenches or clifflike edges with a height of ~ 100 nm (Fig. 17(c)) even though step flow was still maintained locally (Fig. 17(f)) (Ren et al. 2007).

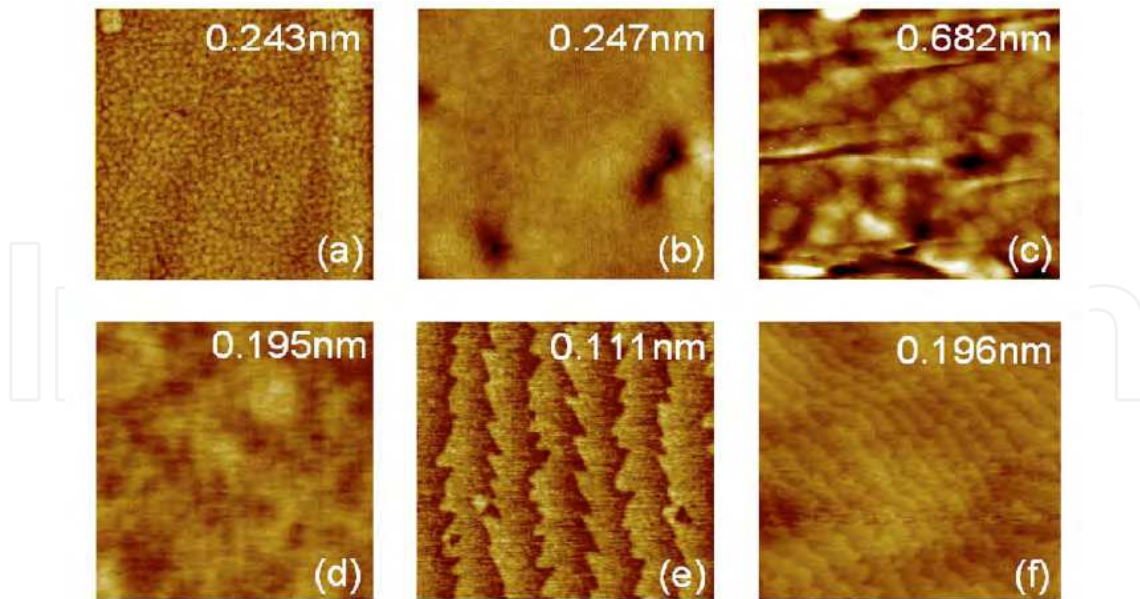


Fig. 17. AFM images of AlGaN superlattices on bulk AlN. The scan area of (a), (b), and (c) is $10 \times 10 \mu\text{m}^2$, and (d), (e), and (f) is $1 \times 1 \mu\text{m}^2$. (a) and (d), (b) and (e), and (e) and (f) are taken after the growth of superlattices 1, 2, and 3, respectively. Root-mean-square (rms) roughness from each scan is labeled.

5. Investigation of III-nitride devices by AFM

The structure of a lateral blue or green InGaN LED is shown in Fig. 18. To observe the surface of each layer and know what happened after each device processing step, researchers use SEM and AFM to check the surface morphology of the patterned sapphire substrates, as-grown LED wafers, etched n-mesa, ITO and p/n metal.

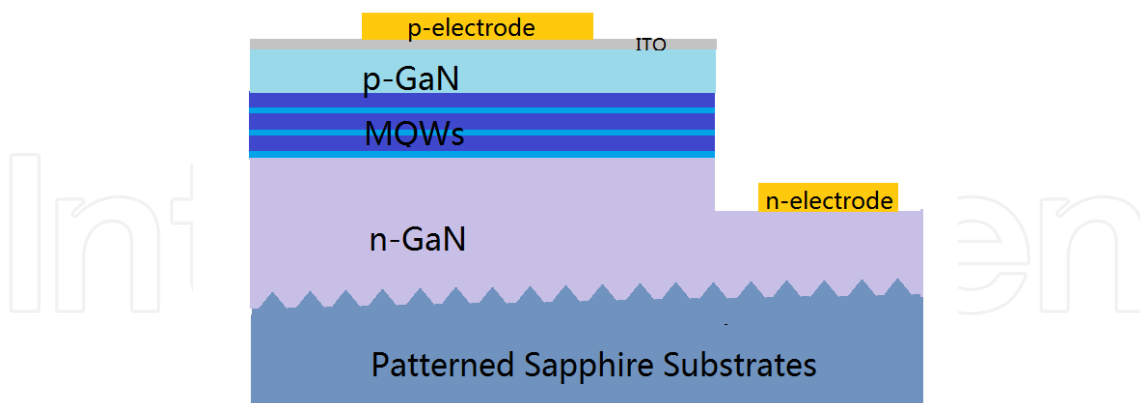


Fig. 18. Structure of a typical lateral GaN based light emitting diode.

5.1 Patterned sapphire substrates

Most of the current commercial LEDs are grown on patterned sapphire substrates (PSS), not on flat sapphire substrates, because LEDs on PSS have demonstrated an enhanced light output power and external quantum efficiency (EQE) compared to conventional LEDs grown on planer sapphire substrates.

LED grown on PSS showed a higher internal quantum efficiency due to a dislocation density reduction by epitaxial lateral overgrowth technology (Tadamoto et al., 2001; Yamada et al., 2002 ; Hsu et al., 2004). Besides the elimination of threading dislocations due to the lateral growth of GaN on top of PSS, researchers believe that PSS improve the light extraction. It is well known that the large difference of refractive index between semiconductor and air leads to trap of large percentage of light emitting from LED (Lee et al., 2005). Thus, it is important to design and characterize the geometry of the PSS. AFM is the only available tool to characterize the bump shape accurately so far.

AFM images of PSS with different specs are shown in Figs. 19(a) and (b). The bump shapes, depths and widths could be characterized accurately. The average bump depth, pitch and gap of the patterns seen in Fig. 19(a) are 1.1 μm , 3 μm and 0.2 μm , respectively. While the average bump depth, pitch and gap of the patterns seen in Fig. 19(b) are 0.3 μm , 6 μm and 3 μm , respectively.

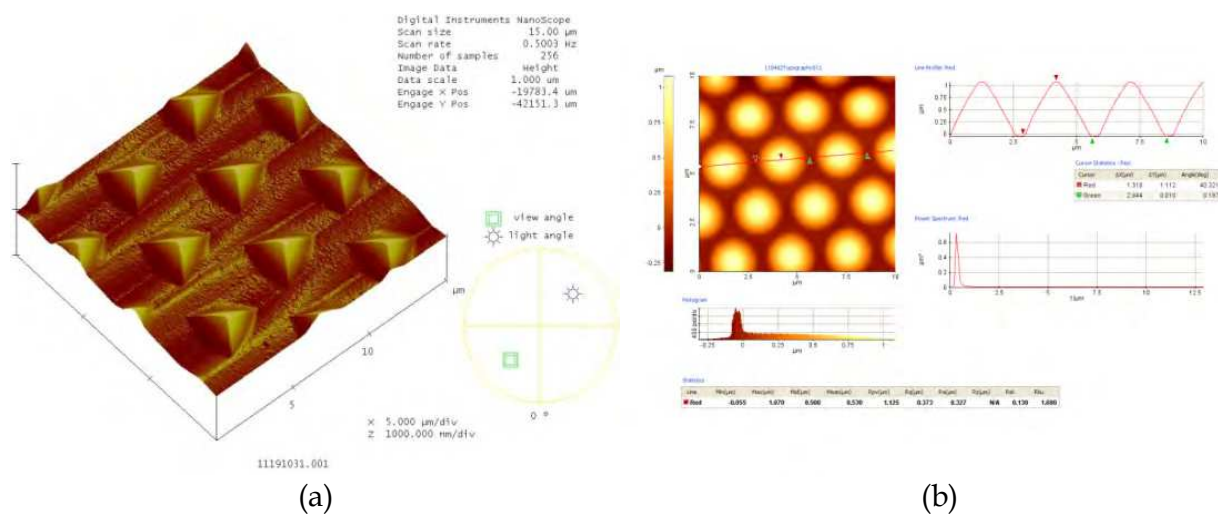


Fig. 19. (a) One patterned sapphire substrate with a cross sectional line to show the height, width and shape of the bumps. (b) 3-dimensional AFM image of another PSS with triangular pyramid cone shaped bumps.

5.2 As grown LED surface and leakage characteristics

Fig. 20 (a) is the surface morphology of an LED grown on a PSS. There is a p++ layer on the top of the LED surface. The bumps on the surface are caused by heavily doped Mg on the surface, usually rooted from a screw type dislocation. In the manufacturing of LEDs it is important to verify that the surface is free of pits, which implies the p-layer has coalesced well and sealed all the V-pits from the underneath layer of InGaN. Fig. 20(b) is an example of a LED with pits on the surface. LEDs with un-coalesced surfaces with pits usually have high leakage currents.

Screw type related pits on the GaN surface have been confirmed to be the source of reverse leakage in GaN films (Law et al., 2010). Fig. 21(a) shows an AFM topograph of a GaN sample grown by molecular beam epitaxy (MBE), in which the screw type TD related pits could be observed. Fig. 21(b)–(d) show conductive atomic force microscopy (CAFM) images obtained at dc biases of -14, -18, and -22 V of the area in Fig. 21(a). Fig. 21(b) shows several small, dark features that correspond to localized reverse-bias leakage paths observable

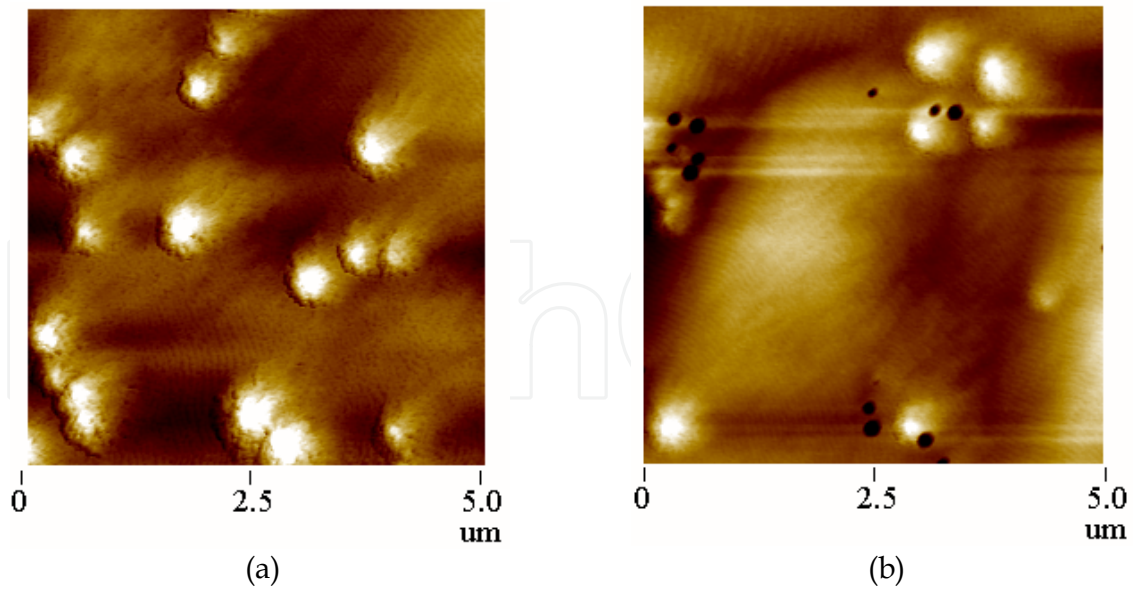


Fig. 20. $5 \times 5 \mu\text{m}^2$ AFM scans of the (a) fully coalesced LED sample and (b) partially coalesced LED sample.

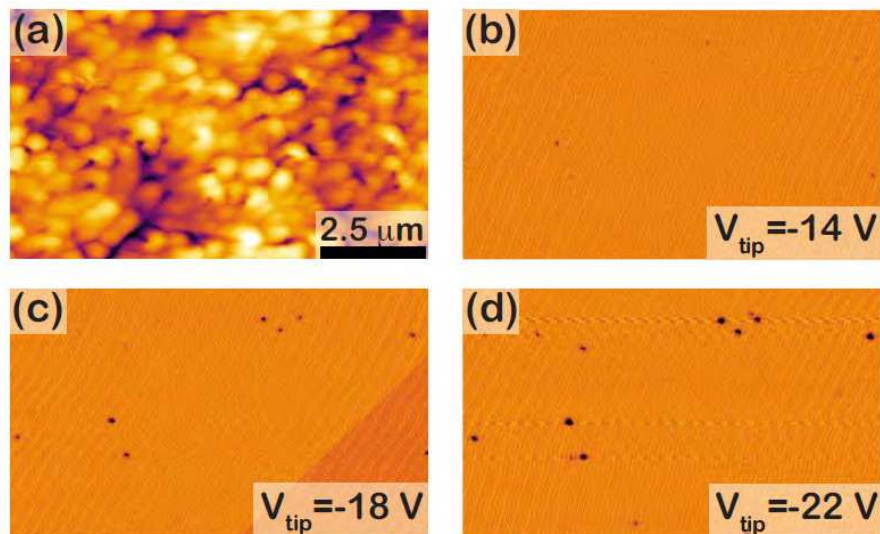


Fig. 21. (a) AFM topograph and (b)–(d) CAFM images obtained at tip dc bias voltages of -14, -18, and -22 V for MBE GaN sample.

at -14 V bias. In Fig. 21(c), the reverse-bias voltage magnitude was further increased and the density of observed conductive paths increased as well. This trend of increasing conductive path density as a function of increasing reverse-bias voltage magnitude continues in Fig. 21(d). According to these results, J. J. M. Law et al. suggested that changes in surface defects surrounding or impurities along screw-component threading dislocations are responsible for their conductive nature (Law et al., 2010).

5.3 Other device processing characterized by AFM

Chemical-mechanical polishing (CMP) is a polishing technique used to thin down the substrates for GaN devices, including Si, SiC, sapphire, AlN and GaN free-standing substrates,

because it may produce high quality surface at low cost and fast material-removal rates. Fig. 22 is a typical $25 \times 25 \mu\text{m}^2$ AFM image of a sapphire substrates polished by CMP.

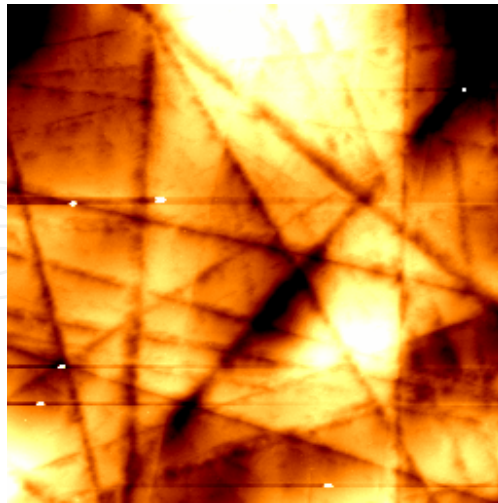


Fig. 22. $25 \times 25 \mu\text{m}^2$ AFM scans of the surface topography of a polished sapphire substrate.

Semi-transparent Ni/ Au on Mg doped GaN was used as the p-contact material in the earlier LED devices. However, the transmittance of such semi-transparent Ni/ Au contact is only around 60 - 75%. Although we could increase the transmittance by reducing Ni/ Au metal layer thickness, the contact reliability could become an issue when the contact layer thickness becomes too small. Transparent indium in oxide (ITO) was popularized as the p-contact material because its high electrical conductivity and transparency to visible light. ITO could be deposited by electron beam evaporation or a magnetron sputtering method. It was found that the LED using sputtering ITO has 2-3% higher Light output (Lop) than that of E-beam ITO. Surface morphology and particle size of the ITO film deposited by two methods were measured by AFM as shown in Fig. 23. AFM analysis helped researchers to better understand the quality difference between the two ITO films. Sputtering ITO was shown to have smaller particle and better uniformity.

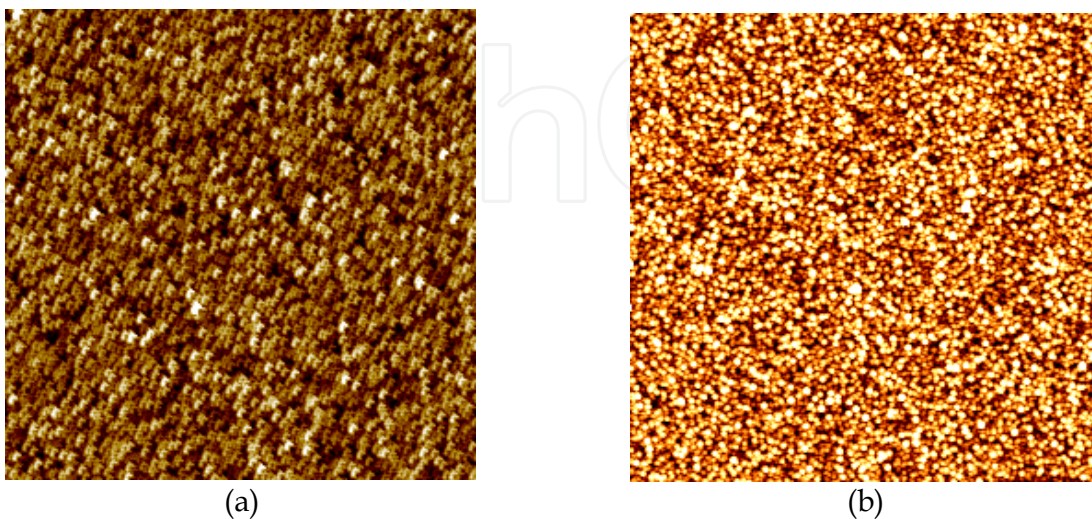


Fig. 23. $5 \times 5 \mu\text{m}^2$ AFM scans of the ITO deposited by (a) electron beam evaporation and (b) magnetron sputtering.

6. Conclusion

In summary, the application of AFM in GaN, In(Ga)N and Al(Ga)N materials research and device fabrication have been reviewed. In regard to the GaN materials, the threading dislocations, including edge, screw and mixed types dislocations, as well as surface features are investigated by AFM. The study of V-shaped defects and topography in InGaN, InN films and InGaN/GaN multiple quantum wells by AFM has been reviewed. For AlN and AlGaN materials, how to utilize AFM to characterize the films and optimize the growth condition are demonstrated. Results also show that AFM is a powerful tool for device characterization and can shed light on device processing optimization.

7. References

- Burton W. K., Cabrera N., & Frank F. C., (1951) *Philos. Trans. R. Soc. London, Ser. A* Vol. 243, pp.299
- Chen, Z., Fareed, R.S.Q., Gaevski, M., Adivarahan, V., Yang, J.W., Mei, J., Ponce, F.A., Khan, M.A. (2006), *Appl. Phys Lett.*, Vol.89, pp. 081905.
- Chen Z., Newman S., Brown D., Chung R., Keller S., Mishra U. K., Denbaars S. P. and Nakamura S., (2008). *Appl. Phys. Lett.*, Vol.93, pp.191906.
- Chen Z., Pei Y., Newman S., Brown D., Chung R., Keller S., Denbaars S. P., Nakamura S. & Mishra U. K., (2009). *Appl. Phys. Lett.*, Vol.94, pp.171117.
- Chen Z., Pei Y., Newman S., Brown D., Chung R., Keller S., Mishra U. K., Denbaars S. P., & Nakamura S. (2009). *Appl. Phys. Lett.*, Vol. 94, pp.112108.
- Cho H. K., Lee J. Y., Yang G. M. & Kim C. S., (2001) *Appl. Phys. Lett.*, Vol.79, pp.215.
- Datta R., Kappers M.J., Barnard J.S., Humphreys C.J., (2004). *Appl. Phys. Lett.* Vol. 85, pp. 3411-3413.
- Detchprohm T., Sano S., Mochizuki S., Kamiyama S., Amano H., & Akasaki I. (2001). *Phys. Status Solidi A*, Vol.188, pp.799.
- Duxbury N., Bangert U., Dawson P., Thrush E. J., Van der Stricht W., Jacobs K., & Moerman I., (2000). *Appl. Phys. Lett.* Vol.76, pp.1600.
- Fischer A.J., Allerman A.A., Crawford M.H., Bogart K.H.A., Lee S.R., Kaplar R.J., Chow W.W., Kurtz S.R., Fullmer K.W., & Figiel J.J. (2004). *Appl. Phys. Lett.*, Vol.84 , pp.3394.
- Follstaedt D.M., Missert N.A., Koleske D.D., Mitchell C.C., Cross K.C., (2003) *Appl. Phys. Lett.* Vol. 83, pp. 4797-4799.
- Gallinat C. S., Koblmüller G., Brown J. S., Bernardis S., Speck J. S., Chern G. D., Readinger E. D. Shen H., & Wraback M., (2006). *Appl. Phys. Lett.* 89, pp.032109.
- Grandusky J. R., Jamil M., Jindal V., Tripathi N., & Shahedipour-Sandvik F. (2007). *J. Vac. Sci. Technol.*, Vol.A 25, pp.441.
- Hsu Y.P., Chang S.J., Su Y.K., Sheu J.K., Lee C.T., Wen T.C., Wu L.W., Kuo C.H., Chang C.S., Shei S.C., (2004). *J. Cryst. Growth* Vol.261 pp. 466-470.
- Hull D. & Bacon D.J., (1984). *Introduction to dislocations*, Pergamon Press, Oxford, pp 71-90.
- Imura M., Nakano K., Fujimoto, N., Okada N., Balakrishnan, K., Iwaya M., Kamiyama S., Amano H., Akasaki I., Noro T., Takagi T., Noro T., Takagi T. & Bandoh A. (2007) *Jpn. J. Appl. Phys.*, Vol. 46, pp.1458.
- Kim I.-H., Park H.-S., Park Y.-J., & Kim T., (1998). *Appl. Phys. Lett.* Vol. 73, pp.1634-1636.

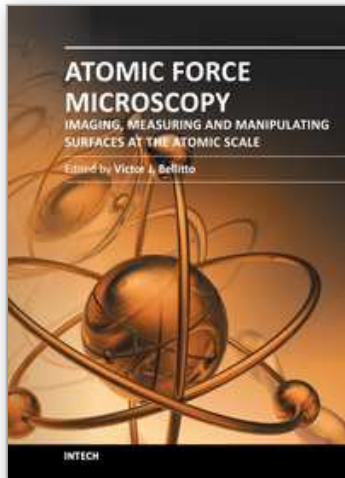
- Kobayashi J. T., Kobayashi N. P., & Dapkus P. D., (1998). Meeting of The American Physical Society, Los Angeles, pp.16–20.
- Koide Y., Itoh N., Itoh, K., Sawaki N., & Akasaki I. (1988). *Jpn. J. Appl. Phys.*, Vol.27, pp.1156 .
- Law J. J. M., Yu E. T., Koblmüller G., Wu F., & Speck J. S., (2010). *Appl. Phys. Lett.* 96, 102111
- Lee Y.J., Hsu T.C., Kuo H.C., Wang S.C., Yang Y.L., Yen S.N., Chu Y.T., Shen Y.J., Hsieh M.H., Jou M.J., Lee B.J., (2005) *Materials Science and Engineering B* Vol.122 pp.184–187
- Li J., Nam K.B., Nakarmi M.L., Lin J.Y., Jiang H.X., Carrier P., & Wei S.H. (2003). *Appl. Phys. Lett.*, Vol.83, pp.5163.
- Lin Y. S., Ma K. J., Hsu C., Feng S. W., Cheng Y. C., Liao C. C., Yang C. C., Chou C. C., Lee C. M., & Chyi J. I., (2000). *Appl. Phys. Lett.* Vol.77, 2988.
- Mayes K., Yasan A., McClintock R., Shiell D., Darvish S.R., Kung P., & Razeghi M. (2004). *Appl. Phys. Lett.*, Vol.84, 1046.
- Northrup J. E., Romano L. T., & Neugebauer J., (1999). *Appl. Phys. Lett.* Vol.74, pp.2319.
- O’Leary S. K., Foutz B. E., Shur M. S., Bhapkar U. V., L Eastman. F., J., (1998). *Appl. Phys.* Vol.83, pp.826.
- Orenberg N. C., Martin M. G., Oliver R. A., Castell M. R., & Briggs G. A. D., (2002). *J. Phys. D: Appl. Phys.* pp.35 615.
- Polyakov V. M. & Schwierz F., (2006). *Appl. Phys. Lett.* Vol.88, pp.032101.
- Ren Z., Sun Q., Kwon S.-Y., Han J., Davitt K., Song Y. K., Nurmikko A. V., Cho H.-K., Liu W., Smart, J. A. & Schowalter L. J., (2007). *Appl. Phys. Lett.*, Vol.91, pp.051116.
- Sangwal K., (1987). *Etching of Crystals*, North-Holland, Amsterdam , pp. 87-160.
- Scholz F., Off J., Fehrenbacher E., Gfrorer O., & Brockt B., (2000). *Phys. Status Solidi A* Vol.180, 315.
- Sharma N., P Thomas., Tricker D., & Humphreys C., (2000). *Appl. Phys. Lett.* Vol.77, 1274.
- Shatalov, M., Chen, Z., Gaevski, M., Adivarahan, V., Yang, J., & Khan, A., (2006). *International Workshop on Nitride Semiconductors*, Kyoto, Japan., pp.101.
- Sun C. J., Anwar M. Z., Chen Q., Yang J. W., Khan M. A., Shur M. S., Bykhovski A. D., Liliental-Weber Z., Kisielowski C., Smith M., Lin J. Y., & Jiang H. X., (1997). *Appl. Phys. Lett.* 70, 2978.
- Sun, W.H., Zhang, J.P., Adivarahan, V., Chitnis, A., Shatalov, M., Wu, S., Mandavilli, V., Yang, J.W., & Khan, M.A. (2004). *Appl. Phys. Lett.*, Vol.85, pp.531.
- Tadatomo K., H Okagawa., Ohuchi Y., Tsunekawa T., Imada Y., Kato M., Taguchi T., (2001) *Jpn. J. Appl. Phys.* Vol.40 pp.L583–L585.
- Takeuchi Y., T., Amano H., Akasaki I., Yamada N., Kaneko Y., & Wang S. Y., *Appl. Phys. Lett.* (1998). Vol.72, pp.710
- Taniyasu Y., Kasu M., & Makimot, T. (2006). *Nature*, Vol.441, pp.325.
- Wang X.L., Zhao D.G., Jahn U., Ploog K., Jiang D.S., Yang H. & Liang J.W. (2007). *J. Phys. D: Appl. Phys.*, Vol.40, pp.1113.
- Weimann N.G., Eastman L.F., Doppalapudi D., Ng H.M., & Moustakas T.D. *J. Appl. Phys.*, Vol.83, 3656. (1998).
- Weyher J.L., Macht L., KamleG. r, Borysiuk J., Grzegory I., (2003). *Phys. Stat. Sol. (c)*, Vol.3 pp.21.
- Wickenden, D.K., Barger, C.B., Bryden, W.A., Miragliotta, J., & Kistenmacher, T. J. (1994). *Appl. Phys. Lett.*, Vol.65, pp.2024.

Wu X. H., Elsaas C. R., Abare A., Mack M., Keller S., Petroff P. M., DenBaars S. P., Speck J. S., & Rosner S. J., (1998). *Appl. Phys. Lett.* Vol.72, pp.692-694.

Yamada M., Mitani T., Narukawa Y., Shioji S., Niki I., Sonobe S., Deguchi K., Sano M., Mukai T., (2002). *Jpn. J. Appl. Phys.* Vol.41 pp.L1431-L1433.

IntechOpen

IntechOpen



Atomic Force Microscopy - Imaging, Measuring and Manipulating Surfaces at the Atomic Scale

Edited by Dr. Victor Bellitto

ISBN 978-953-51-0414-8

Hard cover, 256 pages

Publisher InTech

Published online 23, March, 2012

Published in print edition March, 2012

With the advent of the atomic force microscope (AFM) came an extremely valuable analytical resource and technique useful for the qualitative and quantitative surface analysis with sub-nanometer resolution. In addition, samples studied with an AFM do not require any special pretreatments that may alter or damage the sample and permits a three dimensional investigation of the surface. This book presents a collection of current research from scientists throughout the world that employ atomic force microscopy in their investigations. The technique has become widely accepted and used in obtaining valuable data in a wide variety of fields. It is impressive to see how, in a short time period since its development in 1986, it has proliferated and found many uses throughout manufacturing, research and development.

How to reference

In order to correctly reference this scholarly work, feel free to copy and paste the following:

Z. Chen, L.W. Su, J.Y. Shi, X.L. Wang, C.L. Tang and P. Gao (2012). AFM Application in III-Nitride Materials and Devices, Atomic Force Microscopy - Imaging, Measuring and Manipulating Surfaces at the Atomic Scale, Dr. Victor Bellitto (Ed.), ISBN: 978-953-51-0414-8, InTech, Available from:
<http://www.intechopen.com/books/atomic-force-microscopy-imaging-measuring-and-manipulating-surfaces-at-the-atomic-scale/afm-application-in-iii-nitride-materials-and-devices>

INTECH
open science | open minds

InTech Europe

University Campus STeP Ri
Slavka Krautzeka 83/A
51000 Rijeka, Croatia
Phone: +385 (51) 770 447
Fax: +385 (51) 686 166
www.intechopen.com

InTech China

Unit 405, Office Block, Hotel Equatorial Shanghai
No.65, Yan An Road (West), Shanghai, 200040, China
中国上海市延安西路65号上海国际贵都大饭店办公楼405单元
Phone: +86-21-62489820
Fax: +86-21-62489821

© 2012 The Author(s). Licensee IntechOpen. This is an open access article distributed under the terms of the [Creative Commons Attribution 3.0 License](#), which permits unrestricted use, distribution, and reproduction in any medium, provided the original work is properly cited.

IntechOpen

IntechOpen